1 Project findings

We summarize our project findings on DG methods for the three-dimensional shallow water equations, bed morphology, and non-phase resolving wave models, the use of quadrilateral and triangular elements in the context of DG methods, and the development of an automatic unstructured mesh generation tool below.

1.1 DG methods for the three-dimensional shallow water equations

We have developed a novel DG method for the three-dimensional shallow water equations. In standard Cartesian-coordinates, $(\tilde{x}, \tilde{y}, \tilde{z})$, these equations, which consist of the continuity equation and the equations of horizontal momentum balance, take the form

$$\frac{\partial \tilde{u}}{\partial \tilde{x}} + \frac{\partial \tilde{v}}{\partial \tilde{y}} + \frac{\partial \tilde{w}}{\partial \tilde{z}} = 0$$

$$\frac{\partial \tilde{u}}{\partial \tilde{t}} + \tilde{u}\frac{\partial \tilde{u}}{\partial \tilde{x}} + \tilde{v}\frac{\partial \tilde{u}}{\partial \tilde{y}} + \tilde{w}\frac{\partial \tilde{u}}{\partial \tilde{z}} - f\tilde{v} = -g\frac{\partial \zeta}{\partial \tilde{x}} + \frac{\partial}{\partial \tilde{z}}\left(\tilde{\mu}\frac{\partial \tilde{u}}{\partial \tilde{z}}\right)$$

$$\frac{\partial \tilde{v}}{\partial \tilde{t}} + \tilde{u}\frac{\partial \tilde{v}}{\partial \tilde{x}} + \tilde{v}\frac{\partial \tilde{v}}{\partial \tilde{y}} + \tilde{w}\frac{\partial \tilde{v}}{\partial \tilde{z}} + f\tilde{u} = -g\frac{\partial \zeta}{\partial \tilde{y}} + \frac{\partial}{\partial \tilde{z}}\left(\tilde{\mu}\frac{\partial \tilde{v}}{\partial \tilde{z}}\right)$$

where $\tilde{u}$, $\tilde{v}$, and $\tilde{w}$ are the velocity components in the $\tilde{x}$, $\tilde{y}$, and $\tilde{z}$ directions, respectively, ζ is the free surface elevation measured from still water level, f is the Coriolis parameter, g is gravitational acceleration, and $\tilde{\mu}$ is a vertical eddy viscosity coefficient.

These equations are solved over a time-dependent domain $\tilde{\Omega}(t) \subset \mathbb{R}^3$ and subject to the following boundary conditions:

- Free surface boundary conditions at $\tilde{z} = \zeta$

  $$\frac{\partial \zeta}{\partial \tilde{t}} + \tilde{u}(\zeta)\frac{\partial \zeta}{\partial \tilde{x}} + \tilde{v}(\zeta)\frac{\partial \zeta}{\partial \tilde{y}} - \tilde{w}(\zeta) = 0, \qquad \tilde{\mu}\left.\frac{\partial \tilde{\mathbf{u}}}{\partial \tilde{z}}\right|_{\tilde{z}=\zeta} = \tau_s$$

  where $\tilde{\mathbf{u}} = [\tilde{u},\ \tilde{v}\ \tilde{w}]$ is the velocity vector and τ_s is a (specified) surface stress.

- Bottom boundary conditions at $\tilde{z} = -h$

  $$\tilde{\mathbf{u}}(-h)\cdot\mathbf{n} = 0, \qquad \tilde{\mu}\left.\frac{\partial \tilde{\mathbf{u}}_{\mathbf{xy}}}{\partial \tilde{z}}\right|_{\tilde{z}=-h} = C_f \tilde{\mathbf{u}}_{xy}\,\|\tilde{\mathbf{u}}_{xy}\|$$

  where $\mathbf{n} = [n_x,\ n_y,\ n_z]$ is an outward unit vector normal to the boundary, $\tilde{\mathbf{u}}_{xy} = [\tilde{u},\ \tilde{v}]$ is the horizontal velocity vector, and C_f is a friction coefficient.

- Lateral boundary conditions: We currently consider two types of lateral boundary conditions:

  1. Land boundary: No-normal flow
     $$\tilde{\mathbf{u}}\cdot\mathbf{n} = 0$$
  2. Open ocean boundary: Prescribed surface elevation ζ_o
     $$\zeta = \zeta_o(x, y, t)$$

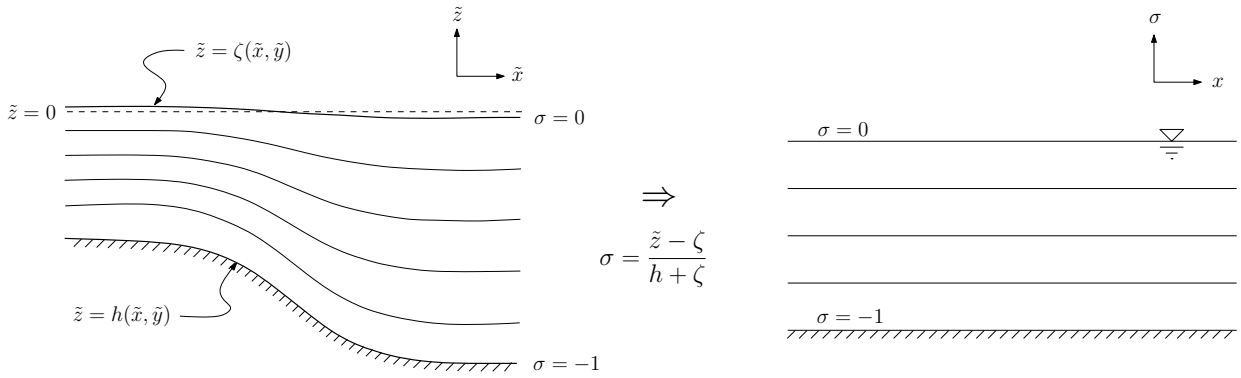

Our DG formulation makes use of discontinuous polynomial spaces of arbitrary order for all the primary variables, including the free surface elevation. In a standard Cartesian-coordinate system, this results in elements at the free surface having mismatched lateral faces (a staircase boundary). This difficulty is avoided in the current method by employing a so-called sigma-coordinate system, which transforms both the free surface and bottom boundaries into coordinate surfaces. This transformation is given by

$$x = \tilde{x}, \quad y = \tilde{y}, \quad \sigma = \frac{\tilde{z} - \zeta}{h + \zeta}, \quad t = \tilde{t}. \tag{1}$$

Note that this transformation gives $\sigma = 0$ at the free surface ($\tilde{z} = \zeta$) and $\sigma = -1$ at the bottom ($\tilde{z} = -h$); see Figure 1. Derivatives of a function $\tilde{f}(\tilde{x}, \tilde{y}, \tilde{z}, \tilde{t}) = f(x, y, \sigma, t)$ with respect to the original coordinates $(\tilde{x}, \tilde{y}, \tilde{z}, \tilde{t})$ are related to derivatives in the new coordinates (x, y, σ, t) by the relations

$$\begin{aligned} \frac{\partial \tilde{f}}{\partial \tilde{x}} &= \frac{\partial f}{\partial x} - \frac{1}{H}\left(\frac{\partial \zeta}{\partial x} + \sigma \frac{\partial H}{\partial x}\right)\frac{\partial f}{\partial \sigma}, & \frac{\partial \tilde{f}}{\partial \tilde{y}} &= \frac{\partial f}{\partial y} - \frac{1}{H}\left(\frac{\partial \zeta}{\partial y} + \sigma \frac{\partial H}{\partial y}\right)\frac{\partial f}{\partial \sigma} \\ \frac{\partial \tilde{f}}{\partial \tilde{z}} &= \frac{1}{H}\frac{\partial f}{\partial \sigma}, & \frac{\partial \tilde{f}}{\partial \tilde{t}} &= \frac{\partial f}{\partial t} - \frac{1}{H}\left(\frac{\partial \zeta}{\partial t} + \sigma \frac{\partial H}{\partial t}\right)\frac{\partial f}{\partial \sigma} \end{aligned} . \tag{2}$$

where $H = \zeta + h$ is the total depth of the water.

Using these relations, the equations in sigma-coordinates can be written in the form

$$\frac{\partial \zeta}{\partial t} + \frac{\partial Hu}{\partial x} + \frac{\partial Hv}{\partial y} + \frac{\partial \omega}{\partial \sigma} = 0. \tag{3}$$

$$\frac{\partial Hu}{\partial t} + \frac{\partial Hu^2}{\partial x} + \frac{\partial Huv}{\partial y} + \frac{\partial u\omega}{\partial \sigma} - fHv = -gH\frac{\partial \zeta}{\partial x} + \frac{\partial}{\partial \sigma}\left(\frac{\mu}{H}\frac{\partial u}{\partial \sigma}\right) \tag{4}$$

$$\frac{\partial Hv}{\partial t} + \frac{\partial Huv}{\partial x} + \frac{\partial Hv^2}{\partial y} + \frac{\partial v\omega}{\partial \sigma} + fHu = -gH\frac{\partial \zeta}{\partial y} + \frac{\partial}{\partial \sigma}\left(\frac{\mu}{H}\frac{\partial v}{\partial \sigma}\right) \tag{5}$$

where ω is the transformed vertical velocity (physically, this is the velocity component normal to the sigma surfaces). The boundary conditions undergo a similar transformation.

DG discretization. The top sigma-coordinate surface, which corresponds to the free surface, is discretized using a two-dimensional triangular mesh that is extended in the vertical direction to produce a three-dimensional mesh of one or more layers of triangular prismatic elements. To

obtain a weak form of the momentum equations we multiply (4) and (5) by arbitrary smooth test functions ϕ, integrate over each element Ω_e, and integrate by parts to obtain

$$\int_{\Omega_e} \frac{\partial \mathbf{Q}}{\partial t}\ \phi\ dV - \int_{\Omega_e} \mathbf{F}(\mathbf{Q})\ \nabla\phi\ dV + \int_{\partial\Omega_e} \mathbf{F}\cdot\mathbf{n}\ dA\ =\ \int_{\Omega_e} \mathbf{s}\ \phi\ dV \tag{6}$$

where $\mathbf{Q} \equiv [Hu,\ Hv]$ and

$$\mathbf{F}\ =\ \begin{bmatrix} Hu^2, & Huv, & u\omega - \mu\dfrac{\partial u}{\partial\sigma} \\ \\ Huv, & Hv^2, & v\omega - \mu\dfrac{\partial v}{\partial\sigma} \end{bmatrix}, \qquad \mathbf{s}\ =\ \begin{bmatrix} fHv - gH\dfrac{\partial\zeta}{\partial x} \\ \\ -fHu - gH\dfrac{\partial\zeta}{\partial y} \end{bmatrix}.$$

Next, we seek to approximate $\mathbf{Q}$, a solution to (6), with a function $\mathbf{Q}_h$ in some finite-dimensional subspace. Thus, we replace $\mathbf{Q}$ by $\mathbf{Q}_h$ in our weak formulation, and we replace the flux function $\mathbf{F}$ in the integrals over interior faces with a suitably chosen numerical flux due to the fact that the approximation spaces used in DG methods do not guarantee continuity across inter-element boundaries. These numerical fluxes must be suitably chosen so that they preserve consistency and stability of the method. In our implementation, we are using the local Lax-Friedrichs flux for the advective numerical fluxes and a local DG (LDG) formulation for the vertical viscosity numerical fluxes; see, for example, [2] for details on the LDG formulation.

An approximation to the free surface elevation is obtained from a weak form of the depth-integrated, sigma-coordinate continuity equation. Depth-integration of (3) (making use of the vertical boundary conditions) yields

$$\frac{\partial\zeta}{\partial t} + \nabla\cdot\bar{\mathbf{Q}} = 0 \tag{7}$$

where $\bar{\mathbf{Q}} = [H\bar{u},\ H\bar{v}]$ is the depth-integrated flux vector. Multiplying (7) by an arbitrary smooth test functions ϕ, integrating over each triangular face of the top layer of elements $\Omega_{e,xy}$, and integrating by parts we obtain

$$\int_{\Omega_{e,xy}} \frac{\partial\zeta}{\partial t}\ \phi\ dA\ -\ \int_{\Omega_{e,xy}} \bar{\mathbf{Q}}\ \nabla\phi\ dA\ +\ \int_{\partial\Omega_{e,xy}} \bar{\mathbf{Q}}\cdot\mathbf{n}\ ds\ =\ 0$$

Again, we obtain a discrete weak form of the problem by replacing ζ with a function ζ_h from some finite-dimensional subspace and by making use of a suitably defined numerical flux for $\bar{\mathbf{Q}}$ along the element edges.

Finally, we obtain the vertical velocity ω by using both the primitive and depth-integrated versions of the continuity equations. Specifically, setting (3) equal to (7), solving for $\frac{\partial\omega}{\partial\sigma}$, replacing $\mathbf{Q}$ and $\bar{\mathbf{Q}}$ by their finite-dimensional approximations, and integrating we obtain

$$\omega_h\ =\ -\int \nabla\cdot\left(\mathbf{Q}_h - \bar{\mathbf{Q}}_h\right)\ d\sigma. \tag{8}$$

Numerical implementation and preliminary results: The polynomial spaces used over the triangular prismatic elements are constructed using a set of orthogonal basis functions defined by

$$\phi_{ijk} = \psi_i^{(1)}\ \psi_{ij}^{(2)}\ \psi_k^{(3)}$$

The so-called principal functions of this basis are defined as

$$\psi_i^{(1)} = P_i^{(0,0)}(\eta_1), \qquad \psi_{ij}^{(2)} = \left(\frac{1-\eta_2}{2}\right)^i\ P_j^{(2i+1,0)}(\eta_2), \qquad \psi_k^{(3)} = P_k^{(0,0)}(\eta_3)$$

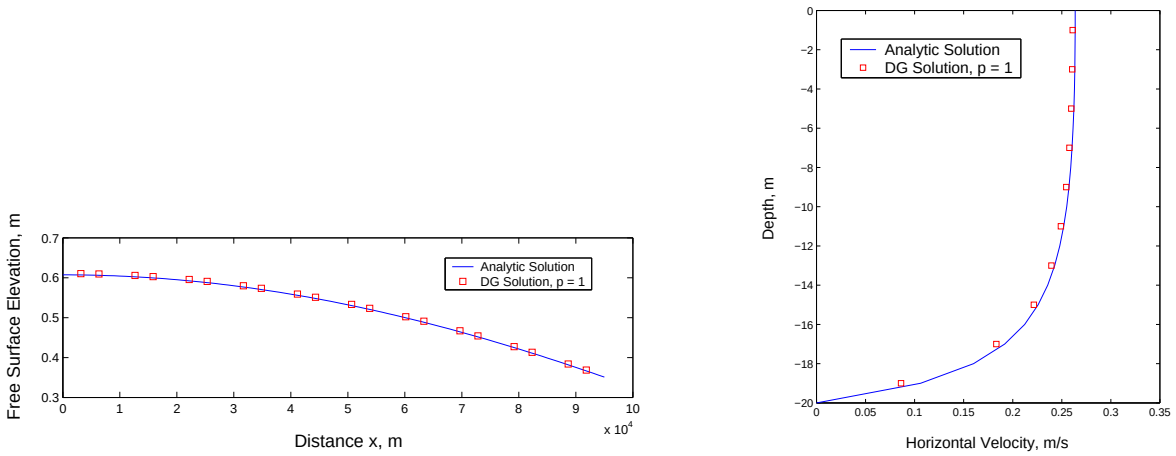

Figure 1: Preliminary numerical results using the proposed DG method showing the free surface elevation (left) and velocity (right) solutions.

where $P_n^{(\alpha,\beta)}$ is the n-th order Jacobi polynomial of weights α and β, and η_1, η_2, and η_3 are a coordinate system defined over a suitably defined reference element.

The use of these basis functions results in several desirable properties in terms of numerical implementation. First, they have the following orthogonality property

$$\int_{-1}^{1}\int_{-1}^{1}\int_{-1}^{-\xi_2} \phi_{ijk}\ \phi_{lmn}\ d\xi_1 d\xi_2 d\xi_3 \ = \ \begin{cases} \left(\dfrac{2}{2i+1}\right)\left(\dfrac{2}{2i+2j+2}\right)\left(\dfrac{2}{2k+1}\right) & \text{if } ijk = lmn \\ 0 & \text{if } ijk \neq lmn \end{cases},$$

which, of course, results in a diagonal mass matrix. Second, the use of this basis results in a very simple form of the discrete depth-averaged flux variables $\bar{\mathbf{Q}}_h$. Specifically, using various properties and identities of the Jacobi polynomials, it can be shown that for N sigma layers we have

$$\bar{\mathbf{Q}}_h \ \equiv \ \int_{-1}^{0} \mathbf{Q}_h \ d\sigma \ = \ \sum_{j=1}^{m} \bar{\mathbf{Q}}_j \ \phi_j^{(2\mathrm{D})} \tag{9}$$

where m is the number of degrees of freedom for a triangular element of a given degree, $\phi_j^{(2\mathrm{D})}$ is a set of orthogonal basis functions for the triangle, which is a subset of the basis functions for the triangular prismatic elements, and $\left\{\bar{\mathbf{Q}}_j\right\}$ is the set of depth-averaged flux degrees of freedom, which are given by

$$\bar{\mathbf{Q}}_j \ = \ \frac{1}{N}\sum_{i=0}^{N-1} \ \mathbf{Q}_j^{(i)}.$$

That is, the degrees of freedom of the depth-averaged flux variables $\bar{\mathbf{Q}}_h$ are simply the average of the appropriate m degrees of freedom of $\mathbf{Q}_h$ over a sigma layer.

Preliminary numerical results of the proposed method applied to an analytic test case for the linear, three-dimensional shallow water equations are shown in Figure (1) using piecewise linear elements. Additional testing and h and p convergence studies are currently underway.

1.2 DG methods for bed morphology

We have developed, analyzed, and implemented a coupled, robust, efficient, parallel DG finite element morphological model designed for two-dimensional unstructured meshes. The model has been implemented within the Advanced Circulation (ADCIRC) modeling framework. Some preliminary code and model verification work has been done. Specifically, we have achieved the following thus far:

- We have formulated the LDG method for the tightly-coupled morphological system, including all diffusion terms, and have derived an *a priori* error estimate for a slightly simplified form of this system.
- We have implemented the tightly-coupled morphological system without the diffusion terms, but with added stabilization terms designed to handle the non-conservative product arising in the momentum equations within the ADCIRC modeling framework [5].
- We have done some preliminary code and model verification work by testing the h- and p-convergence rates against the theoretical rates. This was achieved by comparing the DG model solution against an exact solution [5].
- The model's convergence behavior has been tested, at least qualitatively, on several simplified, idealistic two-dimensional coastal modeling applications. Our observations are compared with those in the literature, where available [5].
- We have added a higher-order slope limiting algorithm to the implementation, which is designed to mitigate spurious oscillations in DG solutions up to order two.

One recent application of the DG morphological model concerns scouring around a bridge pier. In this problem, an initially flat bed is subjected to a uniform, unidirectional flow originating from the western (upstream) boundary. This free stream or upstream velocity is denoted as $\mathbf{u}_\infty = (u_\infty, 0)^T$. The domain under study in this test case is a square of side length 30 m with a circular island of diameter $D = 2$ m positioned at the origin. However, since the true solution $\mathbf{w}$ is symmetric about the x-axis, our domain is chosen as

$$\Omega = \{(x, y) \in \mathbb{R}^2 : x \in (-15, 15), y \in (0, 15), x^2 + y^2 > 1\}$$

in order to save computational time. The bed is initially flat with a depth of 1 m. Boundary conditions are as follows: at $x = -15$, the velocity is fixed at $u_\infty = 0.2$ m/s. At the bridge pile boundary, a no normal flow boundary condition is imposed. No normal flow is also imposed at the top ($y = 15$) and along the axis of symmetry ($y = 0$). At $x = 15$, the free surface elevation is specified as $\zeta = 0$. Below we show results for a DG solution using piecewise quadratic ($p = 2$) solutions. A WENO-type limiter is used for the purpose of enforcing some form of TVB stability.

For this problem, experimental results show that the basic scouring process and flow profile evolution may be summarized as follows. The initial approach flow splits in the horizontal direction when reaching the pier into an upper and lower flow, leaving a stagnation point at the head of the pier (the point $(-1, 0)$ in our domain). A corresponding stagnation pressure results; fluid approaching the stagnation point decelerates, causing some pileup (and thus an increase in ζ) [4] and a bow wave, and then accelerates along the sides of the pier [3]. The fully-developed flow speed along the pier perimeter reaches its maximum at an angle $\theta \approx 75^\circ$ from the pier head, but then separates in the region $90^\circ \leq \theta \leq 120^\circ$ as a result of the acceleration along the sides [7], and a long wake results. Meanwhile, scouring of the bed is initiated near $\theta \approx 75^\circ$, closely corresponding to the

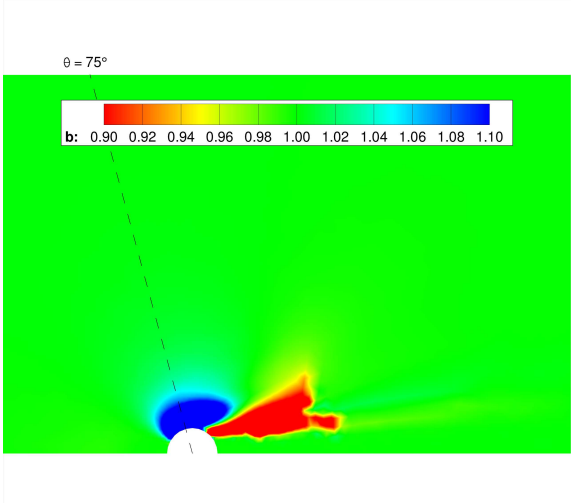

Figure 2: Bed profile after 1 day.

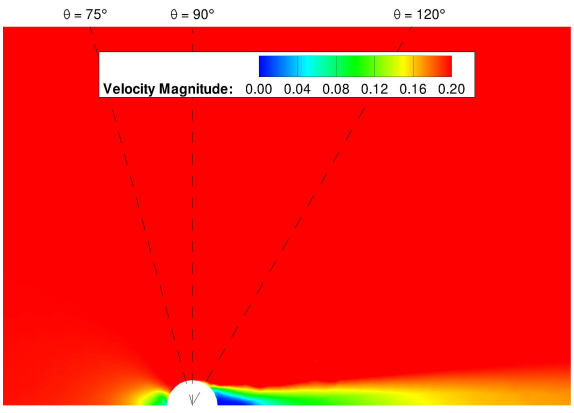

Figure 3: Velocity profile after 1 day.

point where the (attached) accelerating flow reaches its maximum speed [7]. Sediment accretion occurs just downstream of the pier, and the mound slowly drifts downstream with time because of the growing scour hole [7].

However, it should be noted that in addition to this, the approach flow also splits in the vertical direction at the upstream stagnation point; the up-flow contributes to the formation of the bow wave, while the down-flow forms a vertical eddy or vortex [3]. Because of accelerating flow around the pile, a horseshoe vortex system is subsequently formed, and this has been deemed to be the main scouring agent upstream of the pier [3, 7]. Thus, in time, the scour hole advances upstream, eventually becoming U-shaped [3]. We note that this latter process is inherently a three-dimensional effect, and consequently we cannot hope to properly simulate it with our two-dimensional model.

The resulting bed profile is shown in Figure 2. The corresponding velocity profile is displayed in Figure 3. In all results, the locations of the stagnation points, scouring initiation points, points of maximum flow speed along the perimeter, and flow separation points appear to be in good agreement with the results presented in [4] and [7]. In Figure 2, it can be seen that scouring emanates from a point on the pier perimeter near $\theta = 75^\circ$, which agrees with experimental data in [7], and then is deposited just downstream of the pile, as should be expected.

1.3 DG methodology for non-phase resolving wave models

We have studied and implemented finite volume methods for non-phase resolving wave models, with the intent of extending the model to higher order over the next year. As a preliminary test of the model, we have studies the modeling of waves in the presence of an ambient current. As an example, harmonic, long-crested waves are considered propagating from a uniform, upwave boundary (the x-axis) through deep water (10,000m) over a distance of 4,000m with a current that decreases from 0 to -2m/s in the downwave direction. The harmonic waves are simulated with a Gaussian-shaped frequency spectrum with peak frequency 0.1 Hz and standard deviation 0.01 Hz. The long-crestedness is simulated with a $\cos^{500}(\theta)$ directional distribution. The geographic domain is rectangular from 0 to 16,000m with $\triangle x = 640$m in the x-direction and 0 to 4,000m with $\triangle y = 40$m in the y-direction. The directional domain is from 60° to 120° with $\triangle\theta = 1^\circ$. The frequency spectrum is from 0.05 to 0.25 Hz with 41 logorithimcally distributed discrete frequencies.

The analytical solution for this test case is given by [1] [6]:

$$\frac{H^2}{H_i^2} = \frac{c_i^2}{c(c+2U)}$$

$$\frac{c}{c_i} = \frac{1}{2} + 12\left(1 + 4\frac{U}{c_i}\right)^{1/2}$$

pp where H is the wave height and c is the group velocity and i denotes an incident value. The results are shown in Figure (4) and compare the results of our wave model with the analytical solution as well as with the Simulating WAves Nearshore model (SWAN).

1.4 Performance Comparison of Nodal DG on Triangles and Quadrilaterals

In collaborative work with University of Notre Dame on triangular vs. quadrilateral elements for DG methods, we considered the relationship between the accuracy of the approximate solution using different element types and the total computing times used. Figure 5 shows the maximum absolute error in the solution at $t = 0.8$ versus the computing time required to integrate the problem in time. Figure 5(a) reports the results where the triangular meshes are used. The numerical results

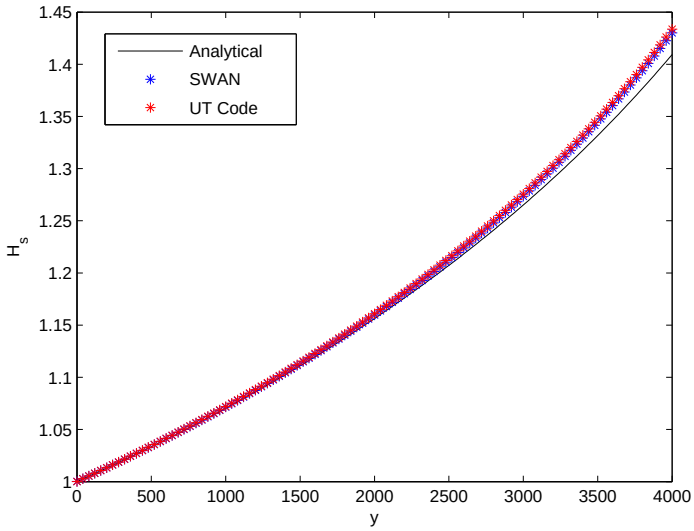

Figure 4: The significant wave height in meters obtain from the exact solution, the UT code, and the SWAN model for the ambient current case.

obtained on the square meshes with the Legendre-Gauss-Lobatto (LGL) nodal set are plotted in Figure 5(b) and with the Legendre-Gauss nodal set in Figure 5(c). Note that each curve is the result of using different levels of resolution. The symbols on each line denote the error for different orders of basis p employed. It can be observed that, as the order p increases, as expected, the computing time required is longer in order to achieve spectral accuracy. The longer run times are a consequence of the use of smaller Δt in the RKF45 (note here we let the RKF45 select the size of Δt automatically). In addition, to obtaining a solution of a certain specified accuracy, the computing time required is shorter for a coarser mesh with a higher order p. In other words, it is more efficient to use a coarser mesh with a higher order p. To see more clearly how the methods compare on the meshes of different resolutions, we plot the error on the mesh of different resolutions when the order p is held fixed against the computing times in Figure 6 for $p = 1$ to 4 and in Figure 7 for $p = 5$ to 8. Note that each line corresponds to a result of a different element type. The symbols on each line represent the three different resolutions. It can be observed that, for the quadrilateral elements, to obtain a certain accuracy, the use of the LG nodal set takes less computing time than that of the LGL nodal set for most cases. In addition, regarding the computing cost to achieve a similar accuracy, the DG solutions on the quadrilateral elements (both square and skewed-rectangular elements) are more efficient than that on the triangular elements. To gain a better idea quantitatively of how these methods compare, we fit, in a least square sense, the log-log plots with a linear function and then calculate from the fitting result a computing time for a required accuracy, denoted as ϵ. Table 1 tabulates the computing times corresponding to the given values of ϵ for different types of elements and the different values of p. Note that the values of ϵ are selected such that they are well in the range of data considered. In this table, a numeric value inside a parenthesis denotes the ratio of the time of the considered method to that of the triangular elements with the same value of order p. From this table, it can be seen that the nodal DG methods using the quadrilateral elements are approximately 1.4 to 5.4 times more efficient than those using the triangular elements for a required accuracy. The quadrilateral elements employing

the LG nodal set are typically two times more efficient than those using the LGL nodal set.

Our numerical results provide clear evidence that there is a benefit in using quadrilateral elements, especially, with the LG nodal set. For a low order p, the methods using the quadrilateral elements would be faster or as fast as the methods using the triangular elements (given that the quadrilateral mesh consists roughly of half as many elements as the triangular mesh) to reach the final time of a simulation. Due to the fact that the nodal basis on a quadrilateral can represent more cross terms of polynomials than the nodal basis on a triangle, it could be expected in general that the approximate solutions from the quadrilateral elements would have better accuracy or, at worst, approximately the same accuracy with those from the triangular elements (which unfortunately we do not know *a priori* for a general problem). This expectation makes the use of the quadrilateral elements particularly appealing for the low to moderate order p since this implies that the methods with the quadrilateral elements would likely be more efficient in order to obtain a required level of accuracy. If the former scenario is the case, the use of quadrilateral elements with higher order p is still appealing due to their higher accuracy per cost as has been shown here.

Table 1: Computing times corresponding to a given value of error ϵ of different types of elements.

Method	Order of basis p							
	1	2	3	4	5	6	7	8
	ϵ =2.0E-1	ϵ =1.0E-2	ϵ =1.0E-3	ϵ =2.0E-4	ϵ =2.0E-5	ϵ =5.0E-6	ϵ =1.0E-6	ϵ =1.0E-7
Tri. Elements[a]	58.01	153.37	415.19	433.69	657.62	635.83	699.61	1121.40
Sq. Elements, LGL[b]	38.54(1.5)	87.74(1.7)	185.56(2.2)	186.05(2.3)	283.57(2.3)	270. 74(2.3)	373.36(1.8)	638.15(1.8)
Sq. Elements, LG[c]	40.18(1.4)	59.98(2.6)	86.39(4.8)	91.80(4.7)	122.76(5.4)	142.52(4.5)	196.93(3.6)	367.58(3.1)
Skewed elements, LGL[d]	41.33(1.4)	91.58(1.7)	177.90(2.3)	214.43(2.0)	294.89(2.2)	336.31(1.9)	414.67(1.7)	742.28(1.5)
Skewed elements, LG[e]	35.21(1.6)	56.97(2.7)	85.02(4.9)	83.85(5.2)	155.12(4.2)	169.49(3.8)	227.57(3.1)	393.41(2.9)

[a] Triangular elements, [b] Square elements with the LGL nodal set, [c] Square elements with the LG nodal set,
[d] Skewed-rectangular elements with the LGL nodal set, [e] Skewed-rectangular elements with the LG nodal set

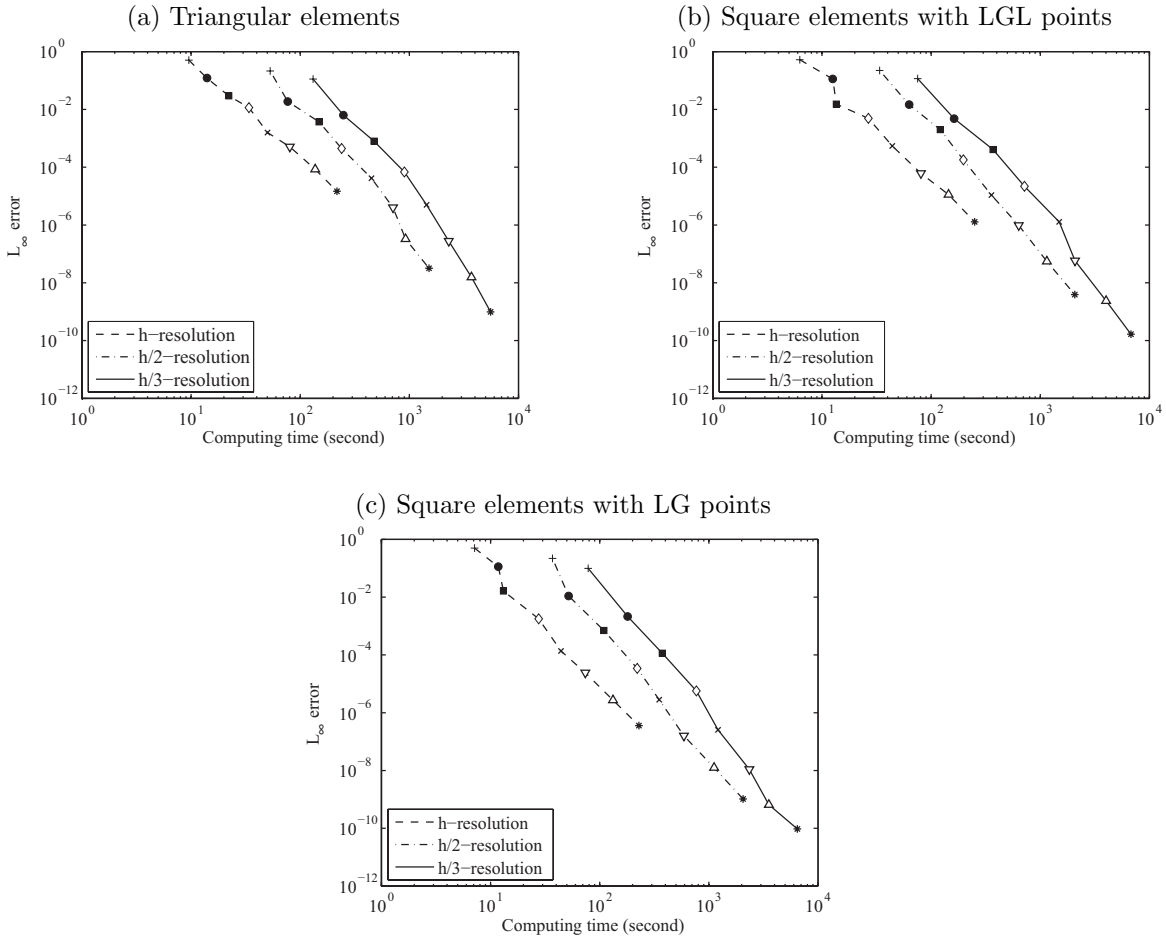

Figure 5: $\|u - u_h\|_{\boldsymbol{\mathcal{N}},\infty}$ at $t = 0.8$ versus computing time (in seconds) used for meshes of three different resolution. (a) triangular elements, (b) square elements with the LGL nodal set, (c) square elements with the LG nodal set. Different symbols represent (successively) solutions for $p = 1$ through $p = 8$.

1.5 Automatic mesh generation

Starting with only a target element size and points defining the boundary and bathymetry / topography of the domain, the goal of the mesh generator being developed is to automatically produce a high-quality mesh from this minimal set of input. From the geometry provided, properties such as local features, curvature of the boundary, bathymetric/topographic gradients, and approximate flow characteristics can be extracted, which are used to determine local element sizes. The result is a high quality mesh, with the correct amount of refinement where it is needed to resolve all of the geometry and flow characteristics of the domain. Techniques incorporated include the use of the so-called signed distance function, which is used to determine critical geometric properties, the approximation of piecewise linear coastline data by smooth cubic splines, a so-called mesh function used to determine element sizes and control the size ratio of neighboring elements, and a force-displacement method which iterates to improve the element quality of the mesh. Figure (1.5) shows a finite element mesh generated automatically using the developed mesh generation tool.

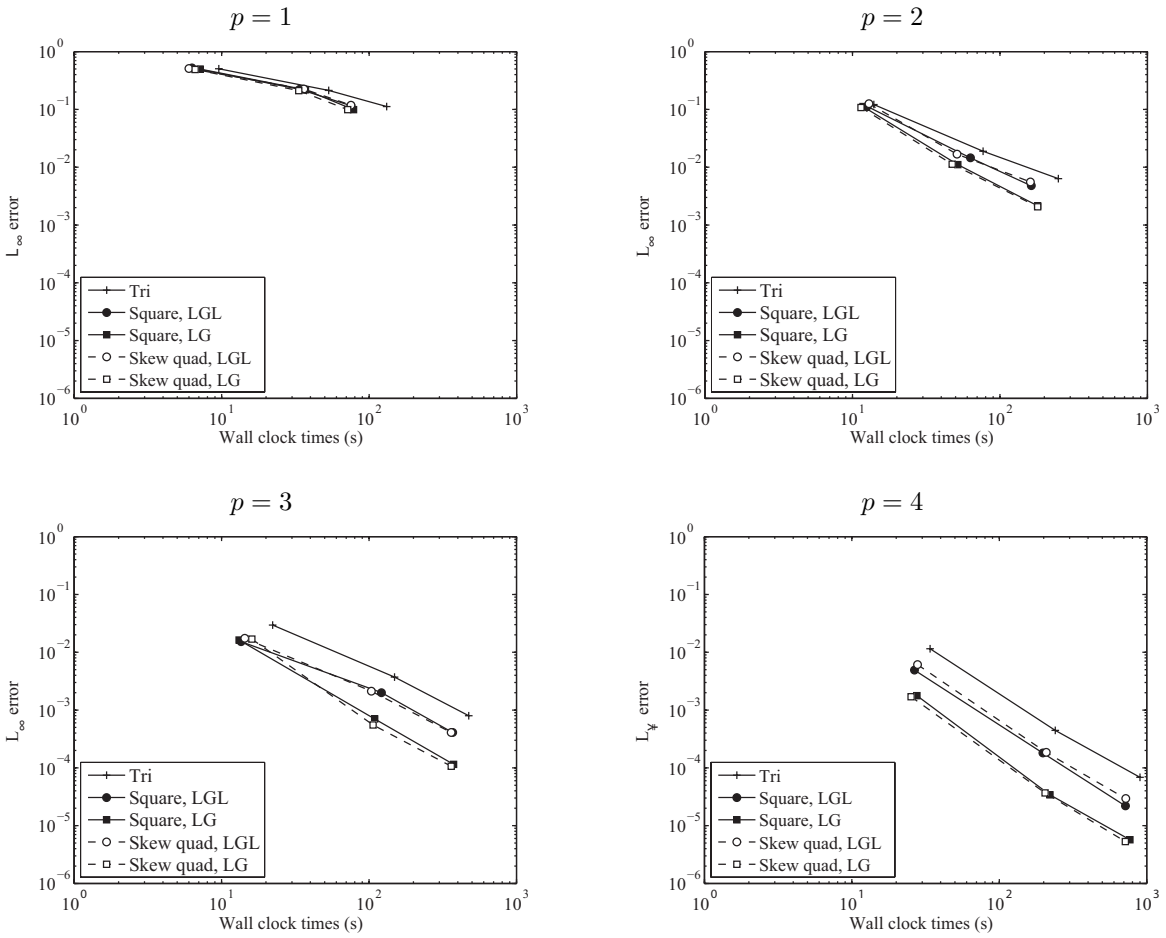

Figure 6: $\|u - u_h\|_{\boldsymbol{\mathcal{N}},\infty}$ at $t = 0.8$ versus computing time (in seconds) used in the methods of different element types of fixed p. (a) $p = 1$, (b) $p = 2$, (c) $p = 3$, and (d) $p = 4$.

References

[1] N. Booij, R.C. Ris, and L.H. Holhuijsen, *A third-generation wave model fro coastal regions. I-Model description and validation*, J. Geophysical Research 104 (1999) 7649–7666.

[2] V. Aizinger , C. Dawson , B. Cockburn , and P. Castillo, *The Local Discontinuous Galerkin Method for Contaminant Transport*, Advances in Water Resources 24 (2000) 73–87.

[3] S. Dey, *Sediment pick-up for evolving scour near circular cylinders*, Appl. Math. Modelling 20 (1996) 534–539.

[4] W. Huang, Q. Yang, and H. Xiao, *CFD modeling of scale effects on turbulence flow and scour around bridge piers*, Comp. Fluids 38 (2009) 1050–1058.

[5] C. Mirabito, C. Dawson, E.J. Kubatko, J.J. Westerink, and S. Bunya, *Implementation of a discontinuous Galerkin Morphological Model on Two-Dimensional Unstructured Meshes*, submitted.

[6] O.M. Phillips, *The Dynamics of the Upper Ocean*, Cambridge University Press, New York, 1977.

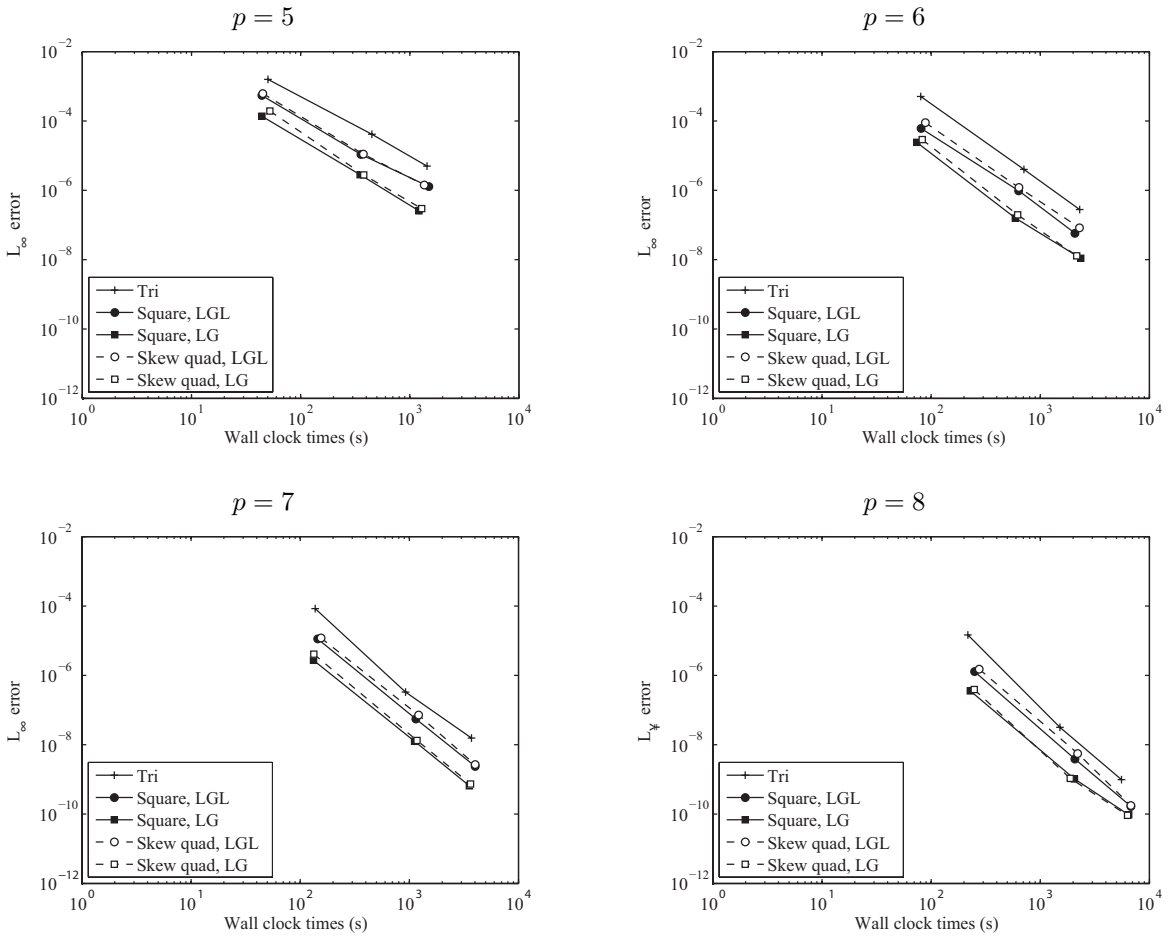

Figure 7: $\|u - u_h\|_{\boldsymbol{\mathcal{N}},\infty}$ at $t = 0.8$ versus computing time (in seconds) used in the methods of different element types of fixed p. (a) $p = 5$, (b) $p = 6$, (c) $p = 7$, and (d) $p = 8$.

[7] J. Unger, W.H. Hager, Down-flow and horseshoe vortex characteristics of sediment embedded bridge piers, Exp. Fluids 42 (2007) 1–19.

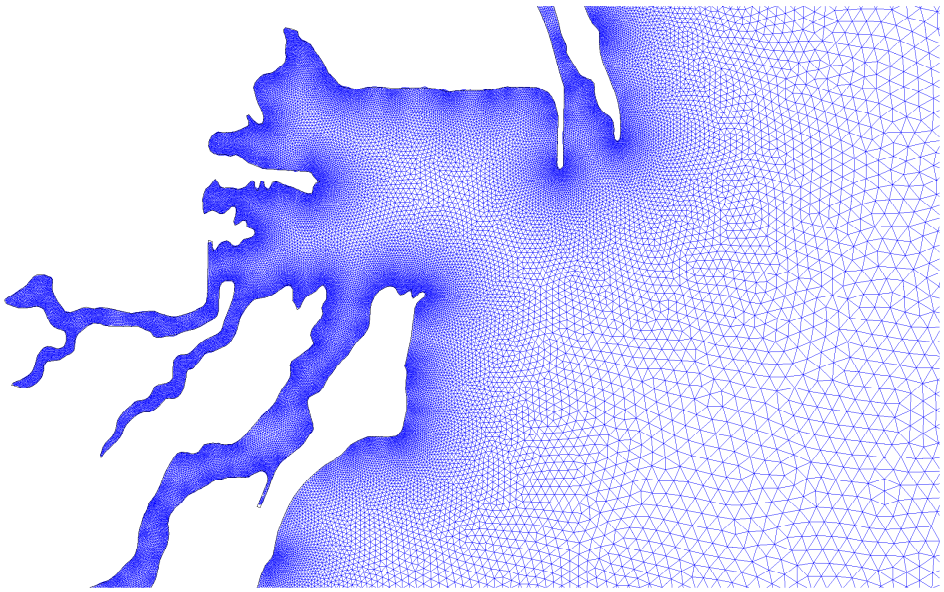

Figure 8: A portion of a finite element mesh along a coastline constructed automatically using the developed automatic mesh generation tool.